Hardening mechanisms of "cold" rolled tungsten after neutron irradiation: indentation and finite elements modelling

Spilios Dellis[1], Xiazi Xiao[2], Dmitry Terentyev[3], Efthymios Manios[1] and Konstantina Mergia[1,*]

[1]National Centre for Scientific Research "Demokritos", Institute of Nuclear and Radiological Science and Technology, Energy and Safety, 15310 Agia Paraskevi, Greece
[2]Department of Mechanics, School of Civil Engineering, Central South University, Changsha 410075, P.R. China
[3]SCK•CEN, Nuclear Materials Science Institute, Boeretang 200, 2400 Mol, Belgium

Abstract

The mechanical properties of "cold" rolled tungsten sheet after neutron irradiation at high temperature are investigated by instrumented indentation and crystal plasticity finite element modelling (CPFEM). Neutron irradiation to a dose of 0.2 displacements per atom was performed in the temperature range from 600 to 1200 ^{o}C in the Belgium material test reactor BR2 at SCK CEN, Mol. The contribution of the irradiation damage in the constitutive laws has been deduced by utilizing the load-depth curves of the indentation measurements and incorporating microstructural information from transmission electron microscopy measurements. The simulated load-depth curves are in very good agreement with the experimental data indicating that the model can characterize the plastic deformation of the irradiated W material. It is found that the irradiation temperature has almost no effect on the load-depth curves and the hardness increases of around 19% after irradiation is temperature independent within errors. The formation of voids after irradiation is the main cause of irradiation induced hardening while the dislocation loops have a much lower influence. Indentation tests at low and high loading rate revealed that void dominated microstructure is more sensitive to the increase of the deformation rate.

Keywords: Tungsten, Plasma facing materials, Neutron irradiation, Radiation damage, Indentation, Crystal plasticity, Finite element method

Corresponding author: Dr Konstantina Mergia, e-mail: kmergia@ipta.demokritos.gr

1 Introduction

The materials of plasma facing components (PFCs) of a fusion reactor have to withstand high energy neutron irradiation, high heat fluxes, the impact of highly energetic particles and cyclic stress loading [1]. Tungsten (W) is the principal candidate material for PFCs application as it possesses high melting temperature, high thermal conductivity, low tritium retention, good sputtering resistance, low swelling, thermal stress and shock resistance, and high-temperature strength of [2, 3]. However, the low fracture toughness and the high brittle to ductile transition temperature (DBTT) of W (100 - 300°C) which are also dependant on microstructure, strain rate and impurity levels [4], are significant drawbacks which have to be addressed for its utmost exploitation. Several methods of microstructural modification have been proposed to alleviate these limitations [5, 6, 7, 8]. Among them "cold" rolling is a promising route as it decreases tungsten's DBTT down to room temperature and increases its strength [9, 10, 11].

As W in PFCs needs to withstand high neuton fluxes numerous campaigns of neutron irradiation of W in fission reactors have been carried out. Neutron irradiation of W results in the formation of vacancy clusters, voids and dislocation loops, as well as chemical composition changes arising from transmutations, *i.e.* production of Re, Os, and Ta. These neutron irradiation defects affect adversely the mechanical properties of the material [12, 13]. The defect structures, concentration and sizes of the different irradiation produced defects versus irradiation temperature and dose have been extensively investigated for irradiation temperature up to 800 ^{o}C [14, 15, 16, 17, 18, 19]. For irradiations at temperatures up to 500 ^{o}C dislocation loops are the main irradiation induced defects, while increase of the dose or temperature promotes the formation of voids [20, 21]. Precipitates and/or clusters of the transmutation products have also been observed after irradiation at doses higher than 1 displacement per atom (dpa) [18, 22, 23, 24]. However, data from neutron irradiation at temperatures higher than 800 ^{o}C are limited even though the plasma facing components are expected to operate at temperatures between 300 and 1200 ^{o}C [3, 25, 26]. To fill this gap several neutron irradiations campaigns have been employed within the European Fusion Project (EUROfusion), targeted to the investigation of neutron irradiation effects on different grades of W material to doses up to 1 dpa and irradiation temperatures up to 1200 ^{o}C [27, 28, 29, 30, 31, 32]. Transmission electron microscopy investigation of W materials, irradiated in one of these campaigns, show that the increase of the irradiation temperature from 600 to 1200 ^{o}C results in the decrease of the density of both dislocation loops and voids and the increase of their size [27, 32].

A powerful tool in the investigation of the mechanical properties of irradiated materials is the instrumented indentation technique (IIT). The advantages of the IIT are that no bulky specimens are required and that information from depths ranging from nm to tens of μm is obtained. The utilization of small volume specimens is significant for the investigations of materials irradiated by fission neutrons as there is limited space in a fission reactor for irradiations [33]. The extended range of depths accessible permits both the study of tungsten after ion irradiation which can generates swallow damage profile (1-2 μm) [34, 35, 36] and after neutron irradiation damaging the whole volume. Therefore, there is an ongoing effort to establish procedures for the assessment of the mechanical properties of materials through IIT [37, 38, 39, 40, 41]. Simulation models based on crystal plasticity theory have been developed utilizing ITT experimental data for the determination of the mechanical properties of materials [42, 43, 44].

In a previous paper, the crystal plasticity finite element method (CP-FEM) model was applied in neutron irradiated tungsten single crystal [45]. In this work, the CP-FEM model is extended to simulate instrumented micro-indentation load-depth curves of W polycrystalline sheet material irradiated to 0.2 dpa, for temperatures ranging from 600 up to 1200 ^{o}C and to deduce the constitutive

laws for the plastic deformation in the presence of irradiation defects. Low and high loading rates were employed to investigate the sensitivity of the material microstructure to the dynamic loading. Data from Transmission Electron Microscopy (TEM) were incorporated as input parameters in the CP-FEM modelling. The various physical mechanisms controlling the hardening of the irradiated W sheet are determined and their contribution to hardening is quantified.

2 Experimental

2.1 Materials and irradiation

The W material was produced by PLANSEE SE in sheet form using a powder metallurgical route consisting of sintering and rolling [46]. The tungsten sintered compact is heated to a temperature of above 1250 °C and it is subsequently rolled to a sheet of thickness 5.5 mm ("hot-rolling"). Next, the sheet is "cold" rolled at a temperature of below 1000 °C and it is brought by progressive rolling steps to a thickness of 1 mm. The resulting material has plate-like grains [27, 47, 48]. Disks were sectioned from the 1 mm thick sheet using electrical discharge machining (EDM). For the removal of surface oxide and surface damage induced by the EDM cutting, both sides of the disk were mechanically polished using diamond suspension up to 0.25 μm and for the final stage colloidal silica. A mirror quality surface was obtained and the final thickness of the samples was reduced to about 0.5 mm. It is noted that due to the fabrication process the texture of the "cold" rolled W sheet specimens varies as a function of depth from the free surface of the 1 mm thick sheet. Electron backscattering diffraction (EBSD) analysis of the cross-section of the unirradiated specimen shows that there is an approximately 500 μm thick volume in the middle of the sheet exhibiting constant texture [45]. Thus, reducing the thickness of the specimens to approximately 500 μm by polishing both of their surfaces results in specimens with small texture variation.

Neutron irradiations were performed at the Belgian Material Test Reactor BR2. The samples were encapsulated in a filled with helium stainless steel tube. The wall thickness (1.5 mm) of the steel tube was designed to act as shielding for the thermal neutrons aiming to attain transmutation rates of W into Re and Os closer to those expected under ITER and DEMO conditions. The irradiations were performed inside a fuel element and in the position of maximum fast neutron flux (7×10^{14} n·cm^{-2}·s^{-1}, $E > 0.1$ MeV). The gap between the samples and the tube was adjusted to achieve the targeted radiation temperature (600, 800, 900, and 1200 °C) based on thermal and neutronic calculations. The irradiation dose was 0.2 displacement per atom (dpa) calculated by MCNPX 2.7.0 for the total fast neutron fluence of 8.9×10^{20} n·cm^{-2} for $E > 0.1$ MeV was reached after three irradiation cycles of a total duration of 70 days [49]. The transmutation of W to Re, Os and Ta according to neutronic calculations, using FISPACT-II inventory code and TENDL-2019 nuclear library have been found in the ranges: 0.54-0.59 at% Re, $(1.3\text{-}1.5)\times10^{-2}$ at% Os and $(2.3\text{-}2.4)\times10^{-3}$ at% Ta.

2.2 TEM

Transmission electron microscopy measurements were carried out using a JEOL 3010 TEM operating at 300 kV. The TEM specimens were cut from the irradiated disks into pieces having a size of about 1.5 × 1.5 × 0.5 mm^3 which were subsequently mechanically polished using SiC paper with grit sizes up to 4000 resulting in sample thickness in the range from 70 to 100 μm. The samples were then glued on 3 mm copper grids with an aperture of 1 mm. Finally, the TEM specimens were electropolished using a aqueous solution of 1.5 wt.% NaOH with an applied voltage of 30 V.

Conventional bright field and dark field diffraction contrast images were recorded mostly under weak beam two beam conditions, while cavities were visualized in out-of-focus imaging conditions. More details about the experimental setup and the method can be found in [27].

2.3 Indentation

Depth-sensing indentation experiments were performed employing NANOVEA's mechanical tester. The maximum applied load was 3 N and the experiments were carried out using two loading/unloading rates of 0.25 N·min^{-1} and 20 N·min^{-1}. A holding time of 200 s was applied in all experiments before the unloading process. A set of nine indentation tests, spaced by 200 μm, were performed. An optical microscope was used to select the indented area free from visible defects.

The Vickers hardness, HV, of the samples was calculated using the contact area, A_C, determined from the optical microscopy images of the resulted imprints, and the mean applied force, F_{max}, during holding time through

$$HV = \frac{F_{\max}}{A_c} = \frac{2F_{\max}}{d_{mean}^2}\sin(\varphi/2), \qquad \text{Eq. 1}$$

where d_{mean} is the mean diagonal of the residual imprint, and φ is the face angle of the square-based diamond pyramid of the Vickers indenter, equal to 136°.

2.4 X-ray diffraction

The crystalline structure was evaluated by X-ray diffraction (XRD) measurements carried out at room temperature using Bruker D8 diffractometer with a Cu K_α X-ray source, a parallel beam stemming from a Göbbel mirror and a scintillator detector.

3 Modelling of the indentation curves

The modelling of the indentation curves is performed by the finite elements method (FEM). For the FEM calculations the code ABAQUS was used together with a user-defined material subroutine (VUMAT) where the tungsten material properties based on the theoretical model of crystal plasticity are implemented. For the definition of the constitutive equations in VUMAT explicit definition of the stress tensor, stress rate and their time dependence are required. Initially a short description of the crystal plasticity theory is given and the different parameters required for the FEM calculations and the sources of these parameters are defined. The values of these parameters have been obtained from the literature and experimental data. The definition of the parameters and the source of their values are given in Table I which should be read in conjunction with the equations describing the crystal plasticity model.

The crystal plasticity model describes the plastic deformation processes by taking into account dislocations gliding along activated slip systems. A slip system a is defined by the unit vector for the slip direction, $\mathbf{s}^a$, and the normal to the slip plane, $\mathbf{n}^a$. In body centred cubic (BCC) metals the

primary slip systems are $\langle 111 \rangle \{110\}$ and $\langle 111 \rangle \{112\}$, i.e. the total number of slip systems is $N_s = 24$ [50]. The viscoplastic strain rate tensor, $\dot{\varepsilon}^{vp}$, is given by [51]

$$\dot{\varepsilon}^{vp} = \sum_{\alpha=1}^{N_s} \mathbf{R}^a \cdot \dot{\gamma}^a = \sum_{\alpha=1}^{N_s} \mathbf{R}^a \left| \frac{\tau^a_{RSS}}{\tau^a_{CRSS}} \right|^{1/m} \operatorname{sgn}\left(\tau^a_{RSS}\right) \qquad \text{Eq.2}$$

where $\dot{\gamma}^a$ is the plastic shear rate, $\mathbf{R}^a = \frac{1}{2}\left(\mathbf{s}^a \otimes \mathbf{n}^a + \mathbf{n}^a \otimes \mathbf{s}^a\right)$ is the Schmid factor tensor and τ^a_{RSS} is the resolved shear stress. The critical resolved shear stress (CRSS), τ^a_{CRSS}, needed to initiate the dislocation slip in the slip system a is the sum of the lattice friction stress, τ_{LF} ,the stress originating from the dislocation-dislocation interaction, τ^a_{SSD}, the Hall-Petch hardening term from grain boundaries, τ_{HP}, and the hardening terms from the irradiation induced dislocation loops (DL), τ^a_{DL} and voids, τ_v. Thus

$$\tau^a_{CRSS} = \tau_{LF} + \tau^a_{SSD} + \tau^a_{DL} + \tau_v + \tau_{HP} \qquad \text{Eq.3}$$

The lattice friction stress, τ_{LF}, for W and temperatures below 580 K can be expressed as [43, 52]

$$\tau_{LF} = \tau_{p0}\left[1 - \sqrt{\frac{k_B T}{2H_k}\ln\left(\frac{\dot{\varepsilon}}{\dot{\varepsilon}_0}\right)}\right] \qquad \text{Eq.4}$$

where k_B is the Boltzmann constant and $\dot{\varepsilon}$ is the loading strain rate defined as in Ref. [43]. (The rest of the parameters are defined in Table I).

The stress due to dislocation-dislocation interaction, τ^a_{SSD}, is considered to follow the dispersed barrier hardening (DBH) based on the Orowan model, i.e.

$$\tau^a_{SSD} = Gbh_{SSD}\sqrt{\rho^a_{SSD}} \qquad \text{Eq.5}$$

where ρ^a_{SSD} is the density of the statistically stored dislocations (SSDs). In BCC crystals, such as W, slip occurs in the closed packed $\langle 1\,1\,1 \rangle$ direction, thus the Burgers vector of a perfect slip dislocation is of the type $\frac{1}{2}\langle 1\,1\,1 \rangle$ [53]. As the plastic deformation progresses the generation and annihilation of SSDs within the plasticity region would result in the evolution of τ^a_{SSD}. This evolution can be described by

$$\dot{\tau}^a_{SSD} = \sum_{\beta=1}^{N_S} h^{a\beta}_{SSD}\dot{\gamma}^\beta - a\sum_{\beta=1}^{N_S}\left|\frac{\tau^\beta_{SSD}}{\tau^{\max}_{SSD}}\right|^{n_0} m^{a\beta}\dot{\gamma}^\beta \qquad \text{Eq.6}$$

where $m^{a\beta}$ is the matrix describing the interaction strength between dislocation gliding in slip systems a and β [54]. τ^β_{SSD} denotes the hardening strength corresponding to the initial density of dislocations, ρ^1_{SSD}, before the indentation starts and $\tau^{\max}_{SSD}$ denotes the maximum SSD hardening strength when the density of the SSDs, $\rho^1_{SSD,saturated}$, is saturated, at the end of the indentation test, which is taken as 10^{15} m^{-2}.

The hardening term, τ_{DL}^{a}, induced by dislocation loops can be expressed as

$$\tau_{DL}^{a} = Gbh_{DL}\sqrt{\rho_{DL}^{\alpha}} \qquad \text{Eq.7}$$

The rate of the dislocation loop hardening term is given by

$$\dot{\tau}_{DL}^{a} = \sum_{\beta=1}^{N_s} h_{DL}^{a\beta}\dot{\gamma}^{\beta} \qquad \text{Eq.8}$$

where $\tau_{DL}^{\max}$, and $\tau_{DL}^{\min}$ are the maximum and minimum dislocation loop hardening strength when the defect density reaches the maximum and minimum values, respectively. The minimum value of the dislocation loop density is taken as one-tenth of the maximum value of N_{DL}, *i.e.* the initial density of DLs before indentation starts. The interaction matrix $\left[n^{a\beta}\right]$ is defined as $n^{a\beta}=1$ when the normal to the slip plane, $\mathbf{n}^{a}$ is not parallel to the normal of the βth habit plane of the DLs, otherwise, $n^{a\beta}=0$. The annihilation of DLs by plastic deformation is considered in the constitutive equations via Eq.8.

The irradiation hardening term, τ_{v}, from voids is considered to follow the Bacon-Kocks-Scattergood (BKS) model [55]

$$\tau_{v} = \frac{Gb}{2\pi L_{void}}\left[\ln\bar{D}+B\right],\ \bar{D}=r_{0}\left[\frac{1}{d_{void}}+\frac{1}{L_{void}}\right] \qquad \text{Eq.9}$$

r_0 is the inner cut-off radius in the energy of dislocation in linear elastic theory and is taken equal to the Burgers vector [56, 57, 58, 59, 60, 61].

Following the Hall-Petch relation [62], τ_{HP} is related to the Hall-Petch coefficient k_{HP} and the mean grain size, d_{grain}, as

$$\tau_{HP} = \frac{k_{HP}}{\sqrt{d_{grain}}} \qquad \text{Eq.10}$$

Table I. Parameters of the constitutive laws for tungsten obtained from the literature.

Parameter	Used in	Value	Ref.
$\dot{\gamma}$, reference shearing rate	Eq.2	10^{-3} s^{-1}	[63]
m, strain rate sensitivity		0.05	
τ_{p0}, reference stress for screw dislocation	Eq.4	1.038 GPa	[52]
H_k, formation enthalpy kink pair on the screw dislocation		$1.65\cdot10^{-19}$ J=0.97eV	
$\dot{\gamma}$, reference strain rate		$3.71\cdot10^{10}$ s^{-1}	
b, Burgers vector	Eq.5,7 & 9	0.274 nm	
G, shear modulus	Eq.5,7 & 9	Table II	Experimental
$\rho_{SSD}^{a}=\rho_{SSD}\ \forall\alpha$, dislocation density	Eq.5	Table II	Experimental

$\rho^{1}_{SSD,saturated}$		10^{-15} m^2	[45]
h_{SSD} , dislocation strength coefficient		0.26	[63]
a_0 , dislocation hardening coefficient	Eq.6	165 MPa	[45]
n_0 , dislocation interaction sensitivity coefficient		4.0	
h_{DL} , defect strength coefficient	Eq.7	0.15	[16]
$\rho^{\alpha}_{DL} = \rho_{DL}\ \forall\alpha$, dislocation loop density		Table II	Experimental
$N^{\min}_{DL}$, minimum dislocation density	Eq.8	0.1 $N^{\max}_{DL}$	
β_0 , dislocation loop hardening coefficient	Eq.8	500 MPa	[45]
n_1 , the defect interaction sensitivity coefficient		2	
L_{void} ,void interspacing	Eq. 9	Table II	Experimental
d_{void} , void diameter		Table II	Experimental
B		1.52	[55]
k_{HP}	Eq.10	3.72 MPa·m$^{1/2}$	[43]

4 Results and Discussion

4.1 Microstructure

The TEM investigation of the reference material has shown that the dislocations are arranged in tangles (Fig.1(a) and (b)) with an average dislocation density of (9.8 ± 2.0)×10^{-13} m^{-2}. The observation of dislocation loops is sporadic with an estimated dislocation density of 6.3×10^{19} m^{-3} and sizes ranging from 3 to 11 nm. The TEM microstructure of the samples irradiated at the temperatures of 600, 800 and 1200 °C has shown that neutron irradiation results in the formation of voids and dislocation loops [27, 28]. Characteristic TEM images are presented in Figure 1(c)-(h). A detailed analysis of the TEM investigation can be found in [27].

The line dislocation density, ρ_{SSD} , number density, N_{DL} and diameter, d_{DL} , of loops and also the number density of voids, N_{void} and their diameter, d_{void} , are presented in Table II. The density of dislocation loops is given as $\rho_{DL} = N_{DL} d_{DL}$ whereas the void interspacing, L_{void} , can be determined by the relation $L_{void} = \frac{1}{\sqrt{N_{void} d_{void}}}$ (Table II).

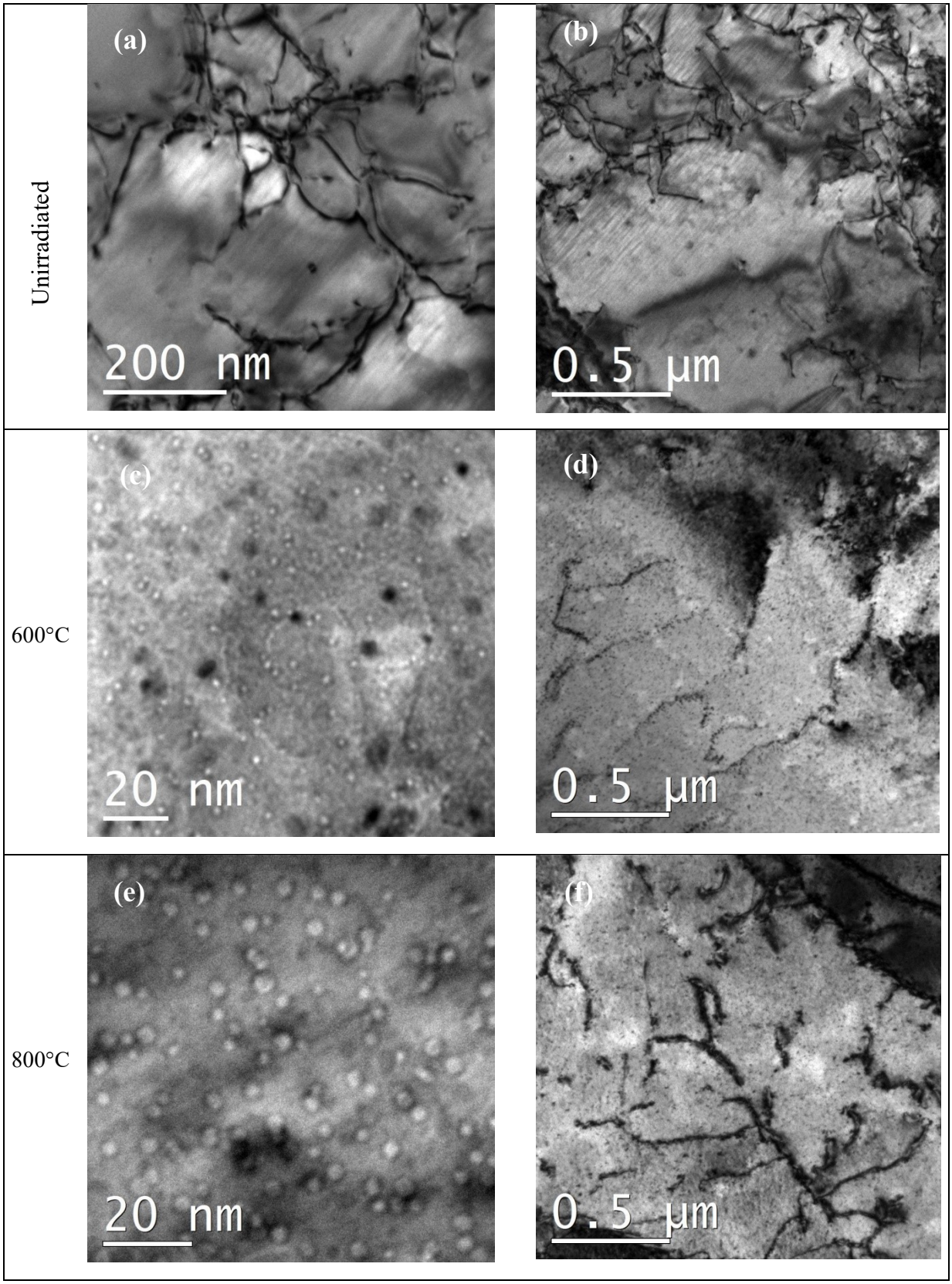
Unirradiated
(a)
200 nm
(b)
0.5 μm
600°C
(c)
20 nm
(d)
0.5 μm
800°C
(e)
20 nm
(f)
0.5 μm

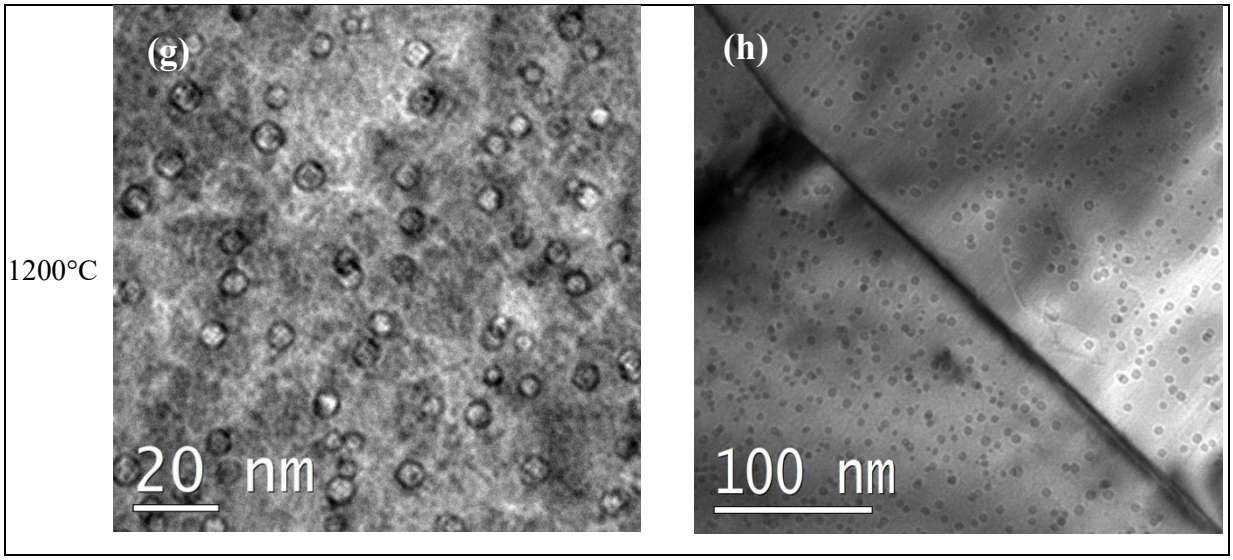

Figure 1. Bright field TEM images of the reference material showing dislocations in high (a) and low (b) magnification, of samples irradiated at 600 °C showing voids (white spots) and loops (dark spots) (c) and decoration of pre-existing dislocation lines with loops (d), of samples irradiated at 800 °C showing voids (white spots) (e) and dislocation loops (dark spots) decorating dislocation lines (f), and of samples irradiated at 1200 °C showing voids (g) and one low angle grain boundary depleted from voids near the interface (h).

The annealing that takes place during the irradiation causes the reduction of the density of the statistically stored dislocation, ρ_{SSD}, from 9.8×10^{13} m^{-2} for the unirradiated material to 1.8×10^{13} m^{-2} at the highest irradiation temperature of 1200 °C. ρ_{SSD} decreases almost linearly with the increase of the irradiation temperature (Table II). Dislocation loops are also observed in the unirradiated W sheet with their diameter ranging between 3 and 11 nm and their density, N_{DL}, being approximately 6.3×10^{19} m^{-3}. Irradiation at 600 °C increases their density to 2.1×10^{22} m^{-3} whereas irradiation at 1200 °C results to a smaller increase of 7×10^{20} m^{-3}. The diameter of the dislocation loops, d_{DL}, is approximately constant and of about 3 nm up to the irradiation temperature of 800 °C and increases to 5.9 nm after irradiation at 1200 °C. Regarding the voids, their number density, N_{void}, decreases by approximately an order of magnitude with the increase of the irradiation temperature, from 1.3×10^{23} m^{-3} at 600 °C to 2×10^{22} m^{-3} at 1200 °C, whereas their diameter, d_{void}, increases with the increase of the irradiation temperature from 1.2 to 3.8 nm, respectively. The shear modulus, G, of the specimens were determined through the impulse excitation technique (IET) [28]. The evolution of the microstructure with the increase of the irradiation temperature and the competing factors of annealing and damage are discussed in more details in [28].

Table II. Dislocation density, dislocation loops and voids of unirradiated and irradiated to 0.2 dpa "cold" rolled W sheet. The data for ρ_{SSD}, N_{DL}, d_{DL}, N_{void} and d_{void} are taken from [27].

T_{irr} (°C)	Dislocations	Dislocation loops			Voids		
	ρ_{SSD} (10^{13} m^{-2})	N_{DL} (10^{22} m^{-3})	d_{DL} (nm)	ρ_{DL} (10^{13} m^{-2})	N_{void} (10^{23} m^{-3})	d_{void} (nm)	L_{void} (nm)
Unirradiated	9.8 ± 2.0	0.0063	3-11	0.14	-	-	-
600	3.5 ± 1.2	2.1 ± 0.9	3.1 ± 1.4	21 ± 13	1.3 ± 0.3	1.2 ± 0.7	80
800	3.1 ± 0.8	0.32 ± 0.05	2.7 ± 0.9	2.7 ± 1.0	0.9 ± 0.2	1.8 ± 0.6	79
1200	1.8 ± 1.0	0.07 ±0.02	5.9 ± 3.9	1.3 ± 0.9	0.2 ± 0.04	3.8 ±1.0	115

The crystal structure of the specimens was investigated by XRD. The XRD patterns of the specimens show bcc crystal structure and that no significant change in the texture of the specimen is induced after irradiation (Figure 2). Small differences between the texture of the unirradiated and irradiated specimens are due to their small thickness difference, since according to EBSD data of 1 mm thick W sheet presented in Ref. [48] the texture varies as a function of depth from the surface of the 1 mm W sheet (see relevant discussion in section 2.1). For the calculation of the volume fraction of the grain orientations from the XRD patterns the relation [64]

$$I_{hkl} = N_{hkl}^{\text{eff}} \cdot m_{hkl} \cdot DW_T(\theta_{hkl}) \cdot |F(\theta_{hkl})|^2 \cdot LP(\theta_{hkl}), \qquad \text{Eq. 11}$$

was used. I_{hkl} is the integrated intensity of the *(hkl)* crystal planes, N_{hkl}^{eff} is the number of crystallites that contribute to the integrated intensity with the direction $\langle hkl \rangle$ perpendicular to the sample surface, F is the structure factor, m_{hkl} is the multiplicity factor, $DW_T(\theta_{hkl})$ is the Debye-Waller factor and $LP(\theta_{hkl})$ the Lorentz-Polarization factor.

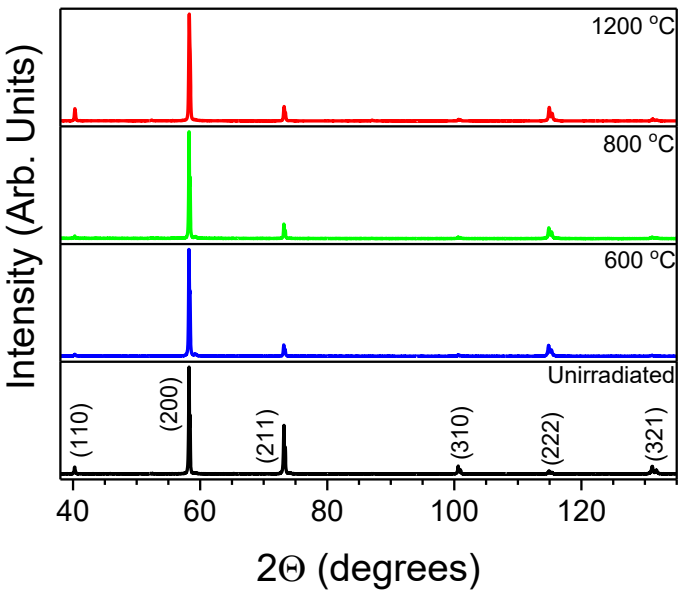

Figure 2. XRD patterns of the unirradiated and irradiated W sheet.

The percentage of [001], [111] and [110] grains for the unirradiated and irradiated samples calculated using Eq.11 are presented in Table III. The percentage of the [001], [111], and [110] grains calculated from the XRD patterns in the present work and those from obtained from the EBSD data in [48] are in general agreement.

From Table III we can conclude that the main orientation of the grains are <100> and <111> and the majority of them (above 65%) are in the <100> orientation. The observed differences in texture (Table III) arise from statistical variations which are due to the fact that the texture depends on depth as it is shown in EBSD measurements [45].

Table III. Crystallite percentages in the crystallographic orientations [001], [111] and [110] for the investigated samples.

T_{irr} (°C)	[001]	[111]	[110]
Unirradiated	87.5	11.5	1
600	64.5	35	0.5
800	65	34.5	0.5
1200	64	35	1

4.2 Hardness and Load-depth curves

In Table IV the shear modulus, G, the Vickers hardness, HV, and the maximum penetration depth, h_{max}, are presented for the two loading rates. The shear modulus has been determined by impulse excitation technique (IET) [28]. It is observed that the irradiation does not change the shear modulus, i.e. the elastic properties of the material. We observe that the hardness for both loading rates is equal within errors. Irradiation at 600 °C induces an 18 % increase in hardness. However, the induced irradiation hardness increase does not depend on irradiation temperature as the hardness for all the irradiated samples is equal within errors. The hardness increase after irradiation is due to the neutron irradiation induced defects, i.e. voids and dislocation loops.

Whereas HV does not differ for the two loading rates, the depth before the creep stage, h_{max}, is different, with that of the higher loading rate being smaller. As it will be discussed below in combination with Figure 4, during the creep stage there is a faster increase of the depth for the higher loading rate which results in equal total penetration depths for both loading rates at the end of creep giving almost equal hardness values.

Table IV. Shear modulus, Vickers hardness and maximum penetration depth for the two loading rates.

		Loading rate 0.25 (N/min)		Loading rate 20 (N/min)	
T_{irr} (°C)	G (GPa)	HV (GPa)	h_{max} (μm)	HV (GPa)	h_{max} (μm)
Unirradiated	158 ± 1	4.76 ± 0.02	4.74 ± 0.01	4.77 ± 0.04	4.53 ± 0.01
600	155 ± 2	5.63 ± 0.06	4.40 ± 0.01	5.61 ± 0.07	4.16 ± 0.01
800	154 ± 2	5.63 ± 0.07	4.40 ± 0.01	5.97 ± 0.06	4.02 ± 0.01
1200	152 ± 2	5.67 ± 0.07	4.36 ± 0.01	5.94 ± 0.08	4.08 ± 0.01

The load-depth curves to be discussed are the average of nine (9) indents. In Figure 3, the load-depth curves of the unirradiated and irradiated W sheet specimens are presented for the loading rate of 0.25 N/min. The load depth curves for all the irradiated samples are quite similar. In order to fully appreciate if the different defect structures as presented in Table II result in different load curves, the difference between the irradiated sample indentation depth from the unirradiated one is plotted versus load in Figure 4 for the 0.25 N/min loading rate. The figure shows that the load-depth of 800 and 1200 °C irradiations are almost the same, whereas these differ from that of the 600 °C with the maximum difference being about 100 nm in depth for loads up to about 1 N.

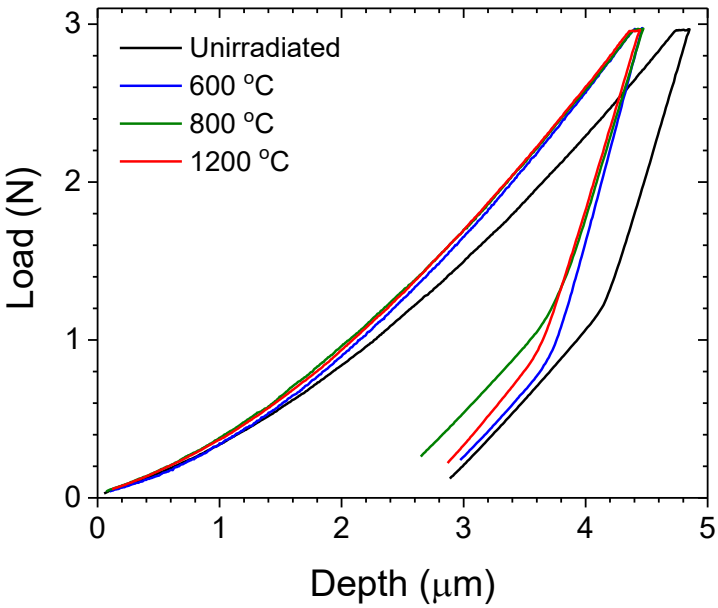

Figure 3. Experimental load-depth curves of Vickers indentation tests on unirradiated and irradiated to 0.2 dpa W "cold" rolled W sheet for 0.25 N/min loading rate.

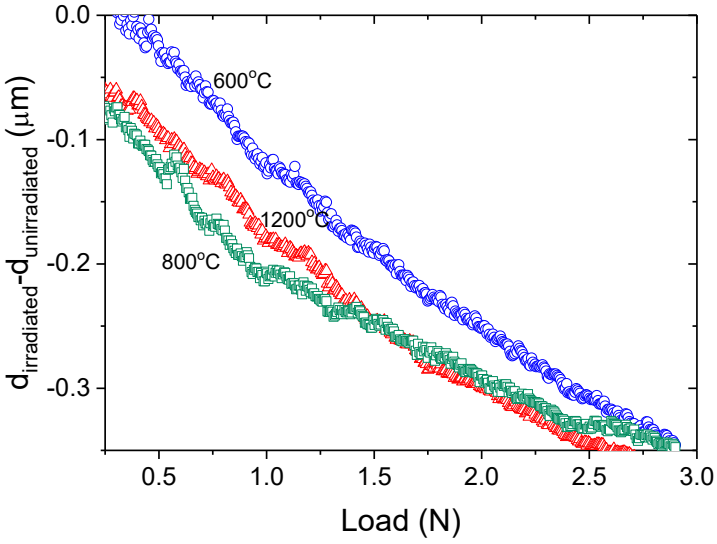

Figure 4. Difference in penetration depth between the irradiated and unirradiated sample as a function of load for 0.25 N/min loading rate.

In Figure 5a, the load-depth curves of the indentation experiments on unirradiated and irradiated W samples at 600, 800, and 1200 °C are presented for the two loading rates of 0.25 and 20 N/min. It is observed that the maximum depth reached at the end of the loading segment and the penetration during the creep stage depend on the loading rate. The maximum penetration depth at the end of the loading stage is smaller the higher the loading rate (Figure 5a). In addition, the loading rate of 0.25 N/min results in an increase of the penetration depth during the creep stage of about 80 nm, over the dwell time of 200 s, whereas for the 20 N/min loading rate the maximum creep depth is around 300 nm (Figure 5b). Furthermore, for the same creep time, as the loading rate decreases the rate at which the depth increases is reduced. This can be understood as follows. During the loading stage with high loading rate, the time is not sufficient for the plastic deformation to be fully developed, i.e. for the dislocations to dissipate away from the stress-concentration indentation zones thereby limiting the plastic strain. This strain is released in the creep stage resulting in high creep depth. On the other hand, when the loading rate is sufficiently low the plastic deformation will be fully developed during the loading stage. This suggests that as the loading rate decreases the response of the material approaches the quasi-static behavior. Similar effects have been observed in [65,66], where the influence of the loading rate and creep time on the calculated hardness and modulus of several bulk and thin film materials was investigated by nanoindentation.

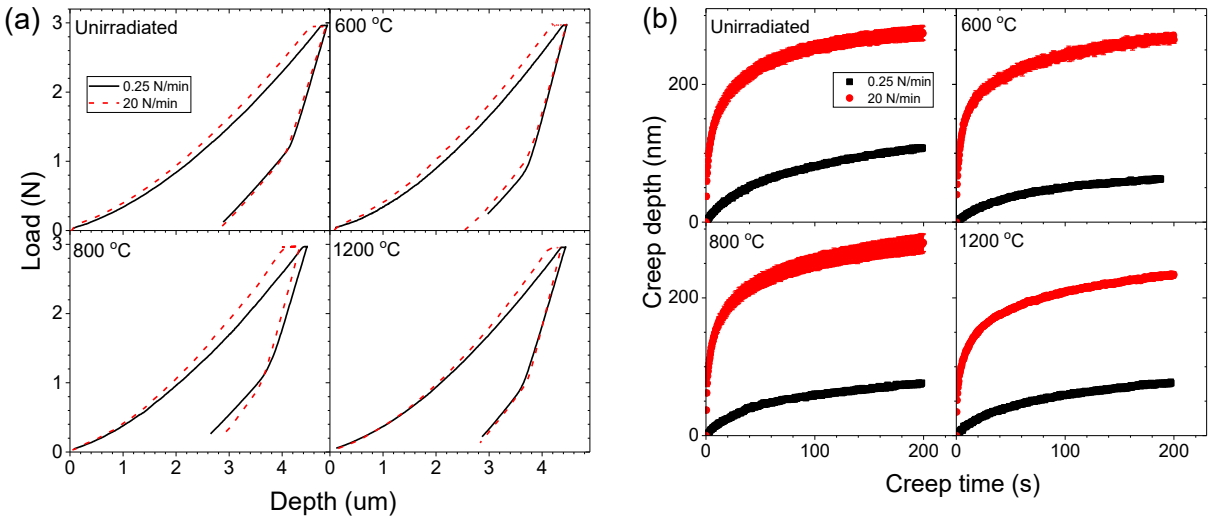

Figure 5. (a) Load-depth curves of unirradiated and irradiated to 0.2 dpa at 600, 900, and 1200 °C with (un)loading rates of 0.25 and 20 N/min. (b) Creep depth-time curves for (un)loading rate for 0.25 and 20 N/min.

4.3 CP-FEM simulation

a) Simulation procedure

The theoretical model described in section 3 is applied to simulate the indentation curves of the W material with the Vickers indenter. The constitutive equations are implemented into the subroutine VUMAT of Abaqus. For the simulations, the sample is simulated by a cylinder with a height of 50 µm and a radius of 50 µm as illustrated in Figure 6(a). The meshed elements for the sample and Vickers indenter are shown in Figure 6(b) and 6(c), respectively. The sample consists of 31212 linear hexahedral elements of type C3D8R and 33696 nodes, and the Vickers indenter is taken as a rigid body meshed with R3D4 elements. For the region beneath the indenter tip, the mesh is refined with the minimum size of 0.1 µm and 0.25 µm along the z-axis direction and in the x-y plane, respectively. The bottom of the sample is fixed and the rest surfaces are free of constraints. The interaction between the sample surface and the indenter tip is set as frictionless as it has little effect on the force-depth relationship [67].

The only parameter of the experimental load-depth curves which is implemented in the FEM calculation is the loading strain rate $\dot{\varepsilon}$ which is introduced via Eq. 4. However, the experimental loading rate is connected with the value of strain rate sensitivity m (Eq. 2). Due to numerical issues, the power-law relationship exponent n ($m = 1/n$) used had the typical value of 20. This value ensures uniqueness in selected deformation systems but much higher values are needed to accurately model the actual material strain-rate sensitivity as it is well known that for most metallic materials the value of n needs to be significantly greater in order to capture their strain-rate sensitive response [68, 69, 70].

The CPFEM model was applied to simulate the experimental indentation load-depth curves for the unirradiated and irradiated W sheet specimens obtained using the low loading rate of 0.25 N/min given that the FEM calculations represent quasi-static load. The constitutive law parameters used for the simulation, as taken from the literature, are presented in Table I, the microstructural

parameters as determined by TEM (available for the irradiation temperatures of 600, 800 and 1200 °C) were taken from [27] and [28] (Table II). CPFEM simulations for the three crystallographic orientations [001], [101] and [111] for these irradiation conditions were performed, and the final load-depth relationship for polycrystalline tungsten was obtained as a weighted sum of the load-depth curves corresponding to the three different orientations.

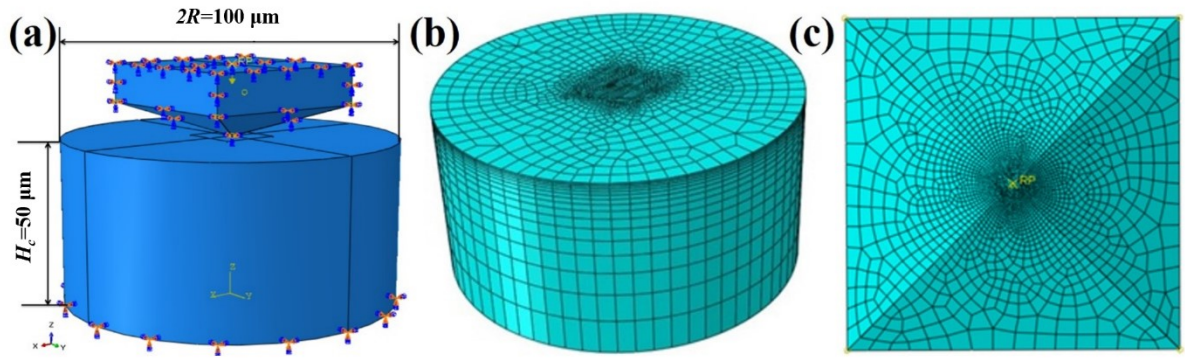

Figure 6. (a) Schematic of the geometrical model for the indentation of tungsten with a Vickers indenter. The indentation is represented as a cylinder with a height of 50 µm and a radius of 50 µm. (b) and (c) The meshes of the sample and the Vickers indenter with the tip radius of 100 nm.

For the simulation of the load-depth curve of the unirradiated specimen three hardening terms, namely the lattice friction stress, τ_{LF}, the dislocation-dislocation interaction term, τ_{SSD}^{a}, and the Hall-Petch hardening term, τ_{HP}, induced by grain boundaries, were considered. TEM results showed a very low density of dislocation loops on the unirradiated specimen that is negligible, and it was not taken into account [27]. These terms have been extensively used for the simulation of the indentation and tensile curves of fusion relevant materials resulting in exceptionally good coincidence between simulation and experimental results [43, 44, 45].

The lattice friction, τ_{LF}, is given by Eq. 4 and using the values of Table I and the experimental strain rate it is calculated and presented in Figure 7. Notwithstanding the strain rate varies strongly with the applied forces the lattice friction due the functional form of Eq. 4 varies reasonably slowly giving mean values for the whole load range with small standard deviation, i.e. $\tau_{LF}(0.25\ \text{N/min})=(404\pm14)$ MPa and $\tau_{LF}(20\ \text{N/min})=(450\pm14)$ MPa .

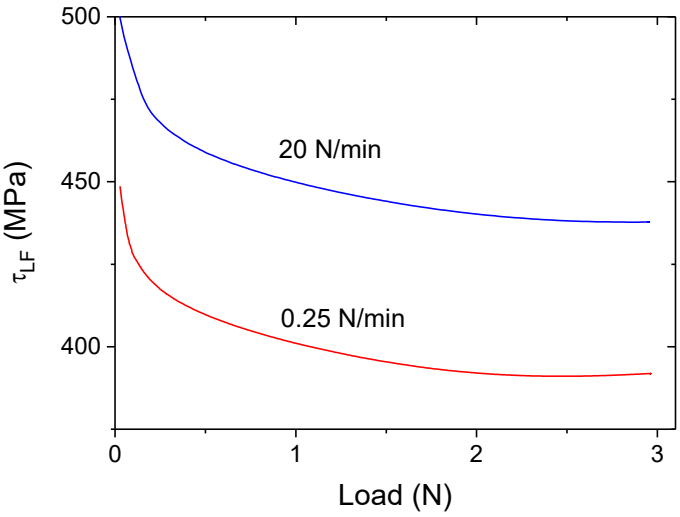

Figure 7. Lattice friction as a function of load for the two loading rates.

The dislocation-dislocation interaction term, τ_{SSD}^{a}, was calculated using Eq.5 and the dislocation line density from TEM measurements (Table II). Finally, the Hall-Petch hardening term, τ_{HP}, was calculated by fitting the simulated curve to the experimental one for the unirradiated specimen.

The simulated curves of the experimental data for the loading segment of the load-depth curve of the unirradiated W sheet are presented in Figure 8a. A good agreement is observed between the simulated curves and experimental data. The obtained value for the Hall-Petch hardening term, τ_{HP}, is (790±68) MPa. From Eq.11 the mean grain size was determined equal to 22 μm, in close agreement with the medium equivalent diameter of the grains derived by Scanning Electron Microscopy (SEM) analysis (~26 μm) [27, 71]. The Hall-Petch hardening term, τ_{HP}, was kept constant for the irradiated specimens as no change in the grain size was observed in the specimens after neutron irradiation [27, 71].

The other terms of CRSS in Eq. 3 have been calculated for the irradiated samples utilizing Table I and TEM results (Table II). Specifically, the hardening term, τ_{DL}, induced by dislocation loops was calculated from Eq.7 and the dislocation loop mean diameter and density, and the irradiation hardening term, τ_{v}, from voids was obtained from Eq. 9 and the void mean diameter and density (Table II). The calculated CRSS stress terms of Eq. 3 are given in Table V. It should be noted that in the calculation the CRSS is the same for all the slip planes and any slip plane dependence comes from eqs. 6 and 8.

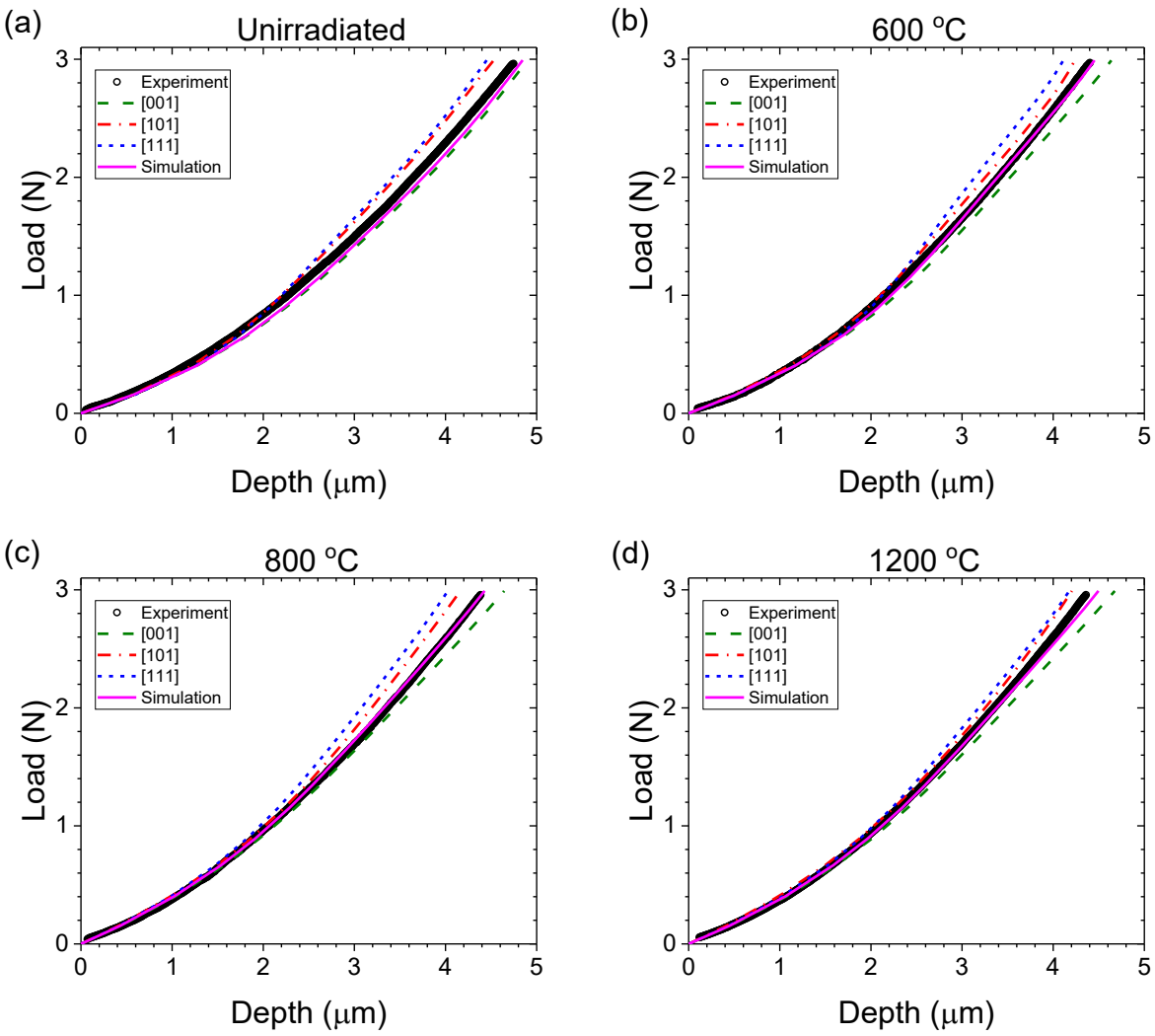

Figure 8. Experimental and simulated (solid line) load-depth curves of Vickers indentation experiments on (a) unirradiated and irradiated to 0.2 dpa at (b) 600 °C, (c) 800 °C, and (d) 1200 °C "cold" rolled W sheet, for (un)loading rate for 0.25 N/min. The simulated load-depth curves for [001] (dashed line), [101] (dot dashed line), and [111] (short dashed line) crystalline orientations are also presented.

The main irradiation induced hardening mechanism is the voids formation as for all irradiation temperatures the τ_v is more than four times higher than τ_{DL} and τ_{SSD}. This finding is consistent with an independent study carried out on single crystal and powder metallurgy tungsten irradiated up to 800 °C [16]. τ_v presents a maximum after irradiation at 800 °C, but it does not change significantly with irradiation temperature. τ_{DL} and τ_{SSD}^{a} have comparable values after irradiation at 600 °C, and they both decrease as the irradiation temperature increases, but τ_{SSD} decreases at a lower rate than τ_{DL}.

The time evolution of the CRSS as indentation proceeds is described by the Eqs. 6 and 8. In order to imitate the experimental indentation curve sequential forces on the indenter are applied and the resulting indenter depth is obtained. Within this approximation time depending effects or relaxation effects are ignored. Thus, the calculation may be considered as quasi-static.

Using the calculated irradiation induced hardening terms, the load-depth curves of the irradiated specimens were simulated and are presented in Figure 8. A good agreement between the simulated and experimental curves is observed supporting the validity of the CPFEM model.

Table V. Calculated stress terms of Eq. 3 using the microstructural data obtained by TEM. For the Hall-Petch hardening term, τ_{HP}, the value obtained from the FEM simulations is presented.

T_{irr} (°C)	τ_{LF} (MPa)	τ_{SSD} (MPa)	τ_{DL} (MPa)	τ_{v} (MPa)	τ_{HP} (MPa)
Unirradiated	Loading rate 0.25 N/min	111 ± 11	-	-	790 ± 68
600	389 ± 5	65 ± 11	52 ± 16	252 ± 79	
800	Loading rate 20 N/min	61 ± 8	19 ± 4	289 ± 58	
1200	440 ± 5	46 ± 13	13 ± 5	238 ± 40	

The obtained here results and specifically the evidence of the high contribution to the irradiation induced hardening coming from the voids signifies the importance of a negative synergistic effect of void swelling which will simultaneously provoke dimensional changes (swelling), loss of thermal conductivity (overheating) and embrittlement (reduced fracture toughness). The region to be exposed to these changes should be located around the temperature corresponding to the peak of the void swelling, which is 800 °C in the case of pure W. Correspondingly, the development of the W-based alloys or other refractory alloys (e.g. high entropy alloys) with an improved resistance against void swelling may have important consequence for operational lifetime of the PFC components.

In the design stage of a Fusion reactor and for the lifetime management of different components, modelling at the macroscopic level of the mechanical behaviour under various irradiation conditions (given the thickness of the in-vessel components), temperatures and loads is required. For this the constitutive equations describing the material response to external loads is a prerequisite.

5 Summary and Conclusions

Instrumented indentation measurements were performed on "cold" rolled W sheet specimens neutron irradiated at 600, 800 and 1200 °C using two (un)loading rates of 0.25 N/min and 20 N/min. The penetration depth depends on the loading rate and the higher the loading rate the lower the penetration depth, which reflects the strain rate sensitivity of the material resistance being usually a feature of ductile material (which is the case of the studied W sheet known to exhibit ductility at room temperature). Neutron irradiation results in an increase of the hardness by approximately (19 ± 2) % for the low (un)loading rate of 0.25 N/min, and this increase shows no dependence on the irradiation temperature. The use of a higher loading rate of 20 N/min does not cause a change in the hardness value of the unirradiated and irradiated at 600 °C specimens as compared to its corresponding value for the (un)loading rate of 0.25 N/min. For the samples irradiated at higher temperatures, a slight increase of the hardness, by approximately 300 MPa, is measured in the case of the high loading rate. This suggests that the void-dominated microstructure, formed at high temperature, is more sensitive to the loading rate as compared to the reference and mixed loop-void microstructure formed at 600 °C.

CPFEM calculations were performed to simulate the loading segments of the load-depth curves of Vickers indentation experiments for the low (un)loading rate, since in the simulations a quasi-static

equilibrium during the loading stage is assumed. The underlying model accounts for the state-of-the art plasticity of non-irradiated polycrystalline W and it incorporates the results from the TEM investigation on the bulk dislocation density, voids, and dislocation loops whose size and density were determined in the irradiated specimens.

In the case of the unirradiated specimen the critical resolved shear stress, τ_{CRSS}, was modelled as the linear superposition of three hardening terms originating from the lattice friction, the dislocation-dislocation interaction term and the interaction of the dislocations with the grain boundaries (Hall-Petch term). The Hall-Petch term was determined to be (790±68) MPa, corresponding to a mean grain size of 22 μm. This is very close to the medium equivalent diameter of the grains derived from the TEM analysis (~26 μm) [27, 71]. Since TEM results show that the irradiation does not result in any change of the grain structure of the specimens, the value of the Hall-Petch term for the simulation of the irradiated specimens was thus kept the same as that used for the reference samples. The strengthening coefficients of the radiation induced defects for CPFEM simulations were accounted for using the TEM obtained microstructural information and an exceptionally good coincidence between the simulated and experimental results was achieved, indicating that the irradiation induced hardness increase can be estimated with good accuracy. The results show that the dominant irradiation hardening comes from the voids, whose fraction becomes maximum after irradiation at 800 °C. The contribution of the voids to the irradiation-induced hardening is five times higher compared to the contribution of the dislocation loops at 600 °C and by eighteen times higher at 1200 °C. Due to the high temperature irradiation, the density of the dislocation lines decreased after irradiation. Correspondingly, the hardening term due to the dislocation-dislocation interaction decreases by a factor of two after irradiation at 600 °C and it decreases even further at 1200 °C.

This work indicates that the plasticity model successfully describes the indentation of W exposed to neutron irradiation in various temperature conditions. For the implementation of the plasticity model in a macroscopic engineering material, the information on the microstructural evolution under irradiation has to be provided, as it has been done in this work. This crucial information may be provided by experimental work or theoretical models which can essentially reduce the time and cost burden otherwise required for the application of transmission electron microscopy.

Acknowledgements

This work has been carried out within the framework of the EUROfusion Consortium and has received funding from the Euratom research and training programme 2014-2018, 2019-2020 and 2021-2025 under Grant Agreements Nos. 633053 and 101052200. The views and opinions expressed herein do not necessarily reflect those of the European Commission. The funding from the General Secretariat of Research and Innovation of the Greek National Programme of the Controlled Thermonuclear Fusion is acknowledged. In addition, Xiazi Xiao acknowledges the support from the National Nature Science Foundation of China (NSFC) under Contract no. 12172384.

1 References

[1] M. Rieth, R. Doerner, A. Hasegawa, Y. Ueda, M. Wirtz, Behavior of tungsten under irradiation and plasma interaction, J. Nucl. Mater. 519 (2019) 334–368. https://doi.org/10.1016/j.jnucmat.2019.03.035

[2] S. Wurster, N. Baluc, M. Battabyal, T. Crosby, J. Du, C. García-Rosales, A. Hasegawa, A. Hoffmann, A. Kimura, H. Kurishita, R.J. Kurtz, H. Li, S. Noh, J. Reiser, J. Riesch, M. Rieth, W. Setyawan, M. Walter, J.H. You, R. Pippan, Recent progress in R&D on tungsten alloys for divertor structural and plasma facing materials, J. Nucl. Mater. 442 (2013) 181–189. https://doi.org/10.1016/j.jnucmat.2013.02.074

[3] G. Pintsuk, Tungsten as a Plasma-Facing Material, in: Compr. Nucl. Mater., Elsevier, 2012: pp. 551–581. https://doi.org/10.1016/B978-0-08-056033-5.00118-X

[4] A. Giannattasio, Z. Yao, E. Tarleton, S.G. Roberts, Brittle-ductile transitions in polycrystalline tungsten, Philos. Mag. 90 (2010) 3947–3959. https://doi.org/10.1080/14786435.2010.502145

[5] J. Riesch, J.Y. Buffiere, T. Höschen, M. Di Michiel, M. Scheel, C. Linsmeier, J.H. You, In situ synchrotron tomography estimation of toughening effect by semi-ductile fibre reinforcement in a tungsten-fibre-reinforced tungsten composite system, Acta Mater. 61 (2013) 7060–7071. https://doi.org/10.1016/j.actamat.2013.07.035

[6] Q. Wei, H.T. Zhang, B.E. Schuster, K.T. Ramesh, R.Z. Valiev, L.J. Kecskes, R.J. Dowding, L. Magness, K. Cho, Microstructure and mechanical properties of super-strong nanocrystalline tungsten processed by high-pressure torsion, Acta Mater. 54 (2006) 4079–4089. https://doi.org/10.1016/j.actamat.2006.05.005

[7] H. Kurishita, S. Matsuo, H. Arakawa, S. Kobayashi, K. Nakai, T. Takida, K. Takebe, M. Kawai, Superplastic deformation in W-0.5 wt.% TiC with approximately 0.1 μm grain size, Mater. Sci. Eng. A. 477 (2008) 162–167. https://doi.org/10.1016/j.msea.2007.05.009

[8] M. Rieth, J. Reiser, B. Dafferner, S. Baumgärtner, The impact of refractory material properties on the helium cooled divertor design, Fusion Sci. Technol. 61 (2012) 381–384. https://doi.org/10.13182/FST12-1T3

[9] J. Reiser, J. Hoffmann, U. Jäntsch, M. Klimenkov, S. Bonk, C. Bonnekoh, M. Rieth, A. Hoffmann, T. Mrotzek, Ductilisation of tungsten (W): On the shift of the brittle-to-ductile transition (BDT) to lower temperatures through “cold” rolling, Int. J. Refract. Met. Hard Mater. 54 (2016) 351–369. https://doi.org/10.1016/j.ijrmhm.2015.09.001

[10] C. Bonnekoh, A. Hoffmann, J. Reiser, The brittle-to-ductile transition in “cold” rolled tungsten: On the decrease of the brittle-to-ductile transition by 600 K to − 65 °C, Int. J. Refract. Met. Hard Mater. 71 (2018) 181–189. https://doi.org/10.1016/j.ijrmhm.2017.11.017

[11] C. Bonnekoh, P. Lied, S. Zaefferer, U. Jäntsch, A. Hoffmann, J. Reiser, M. Rieth, The brittle-to-ductile transition in “cold”-rolled tungsten sheets: Contributions of grain and subgrain boundaries to the enhanced ductility after pre-deformation, Elsevier, 2020. https://doi.org/10.1016/j.nme.2020.100769

[12] L.M. Garrison, Y. Katoh, N.A.P.K. Kumar, Mechanical properties of single-crystal tungsten irradiated in a mixed spectrum fission reactor, J. Nucl. Mater. 518 (2019) 208–225. https://doi.org/10.1016/j.jnucmat.2019.02.050

[13] T. Miyazawa, L.M. Garrison, J.W. Geringer, M. Fukuda, Y. Katoh, T. Hinoki, A. Hasegawa, Neutron irradiation effects on the mechanical properties of powder metallurgical processed tungsten alloys, J. Nucl. Mater. 529 (2019) 151910. https://doi.org/10.1016/j.jnucmat.2019.151910

[14] A. Hasegawa, M. Fukuda, K. Yabuuchi, S. Nogami, Neutron irradiation effects on the microstructural development of tungsten and tungsten alloys, J. Nucl. Mater. 471 (2016) 175–183. https://doi.org/10.1016/j.jnucmat.2015.10.047

[15] A. Hasegawa, T. Tanno, S. Nogami, M. Satou, Property change mechanism in tungsten under neutron irradiation in various reactors, J. Nucl. Mater. 417 (2011) 491–494. https://doi.org/10.1016/j.jnucmat.2010.12.114

[16] X. Hu, T. Koyanagi, M. Fukuda, N.A.P.K. Kumar, L.L. Snead, B.D. Wirth, Y. Katoh, Irradiation hardening of pure tungsten exposed to neutron irradiation, J. Nucl. Mater. 480 (2016) 235–243. https://doi.org/10.1016/j.jnucmat.2016.08.024

[17] R.K. Williams, F.W. Wiffen, J. Bentley, J.O. Stiegler, Irradiation induced precipitation in tungsten based, W-Re alloys, Metall. Trans. A. 14 (1983) 655–666. https://doi.org/10.1007/BF02643781

[18] Y. Katoh, L.L. Snead, L.M. Garrison, X. Hu, T. Koyanagi, C.M. Parish, P.D. Edmondson, M. Fukuda, T. Hwang, T. Tanaka, A. Hasegawa, Response of unalloyed tungsten to mixed spectrum neutrons, J. Nucl. Mater. 520 (2019) 193–207. https://doi.org/10.1016/j.jnucmat.2019.03.045

[19] A. Hasegawa, M. Fukuda, S. Nogami, K. Yabuuchi, Neutron irradiation effects on tungsten materials, Fusion Eng. Des. 89 (2014) 1568–1572. https://doi.org/10.1016/j.fusengdes.2014.04.035

[20] A. Hasegawa, M. Fukuda, T. Tanno, S. Nogami, Neutron irradiation behavior of tungsten, Mater. Trans. 54 (2013) 466–471. https://doi.org/10.2320/matertrans.MG201208

[21] T. Koyanagi, N.A.P.K. Kumar, T. Hwang, L.M. Garrison, X. Hu, L.L. Snead, Y. Katoh, Microstructural evolution of pure tungsten neutron irradiated with a mixed energy spectrum, J. Nucl. Mater. 490 (2017) 66–74. https://doi.org/10.1016/j.jnucmat.2017.04.010

[22] M. Dürrschnabel, M. Klimenkov, U. Jäntsch, M. Rieth, H.C. Schneider, D. Terentyev, New insights into microstructure of neutron-irradiated tungsten, Sci. Rep. 11 (2021) 7572. https://doi.org/10.1038/s41598-021-86746-6.

[23] M.J. Lloyd, R.G. Abernethy, M.R. Gilbert, I. Griffiths, P.A.J. Bagot, D. Nguyen-Manh, M.P. Moody, D.E.J. Armstrong, Decoration of voids with rhenium and osmium transmutation products in neutron irradiated single crystal tungsten, Scr. Mater. 173 (2019) 96–100. https://doi.org/10.1016/j.scriptamat.2019.07.036.

[24] M. Fukuda, K. Yabuuchi, S. Nogami, A. Hasegawa, T. Tanaka, Microstructural development of tungsten and tungsten-rhenium alloys due to neutron irradiation in HFIR, J. Nucl. Mater. 455 (2014) 460–463. https://doi.org/10.1016/j.jnucmat.2014.08.002

[25] T. Hirai, S. Panayotis, V. Barabash, C. Amzallag, F. Escourbiac, A. Durocher, M. Merola, J. Linke, T. Loewenhoff, G. Pintsuk, M. Wirtz, I. Uytdenhouwen, Use of tungsten material for the ITER divertor, Nucl. Mater. Energy. 9 (2016) 616–622. https://doi.org/10.1016/j.nme.2016.07.003

[26] J.H. You, E. Visca, T. Barrett, B. Böswirth, F. Crescenzi, F. Domptail, M. Fursdon, F. Gallay, B.E. Ghidersa, H. Greuner, M. Li, A. V. Müller, J. Reiser, M. Richou, S. Roccella, C. Vorpahl,

European divertor target concepts for DEMO: Design rationales and high heat flux performance, Nucl. Mater. Energy. 16 (2018) 1–11. https://doi.org/10.1016/j.nme.2018.05.012

[27] A. Dubinko, D. Terentyev, C. Yin, W. Van Renterghem, B. Rossaert, M. Rieth, E.E. Zhurkin, A. Zinovev, C.C. Chang, S. Van Dyck, G. Bonny, Microstructure and hardening induced by neutron irradiation in single crystal, ITER specification and "cold" rolled tungsten, Int. J. Refract. Met. Hard Mater. 95 (2021) 105522. https://doi.org/10.1016/j.ijrmhm.2021.105522

[28] K. Mergia, V. Chatzikos, E. Manios, S. Dellis, D. Papadakis, D. Terentyev, G. Bonny, A. Dubinko, I.E. Stamatelatos, S. Messoloras, M. Rieth, Evolution of microstructure in neutron irradiated "cold" rolled tungsten and its correlation with hardness, Fusion Eng. Des. 172 (2021) 112784. https://doi.org/10.1016/j.fusengdes.2021.112784.

[29] D. Terentyev, C. Yin, A. Dubinko, C.C. Chang, J.H. You, Neutron irradiation hardening across ITER diverter tungsten armor, Int. J. Refract. Met. Hard Mater. 95 (2021) 105437. https://doi.org/10.1016/j.ijrmhm.2020.105437

[30] D. Papadakis, S. Dellis, V. Chatzikos, E. Manios, I.E. Stamatelatos, S. Messoloras, K. Mergia, Neutron irradiation effects in different tungsten microstructures, Phys. Scr. 96 (2021) 124041. https://doi.org/10.1088/1402-4896/ac1eb2.

[31] D. Papadakis, S. Dellis, K. Mergia, V. Chatzikos, D. Terentyev, G. Bonny, A. Dubinko, W. Van Renterghem, M. Konstantinovic, S. Messoloras, G. Pintsuk, The competing effects of temperature and neutron irradiation on the microstructure and mechanical properties of ITER grade tungsten, Fusion Eng. Des. 168 (2021) 112608. https://doi.org/10.1016/j.fusengdes.2021.112608.

[32] V. Chatzikos, K. Mergia, G. Bonny, D. Terentyev, D. Papadakis, G.E. Pavlou, and S. Messoloras, Positron annihilation spectroscopy investigation of neutron irradiated tungsten materials, Int. J. Refract. Met. Hard Mater. 105 (2022) 105838 https://doi.org/10.1016/j.ijrmhm.2022.105838

[33] P. Hosemann, Small-scale mechanical testing on nuclear materials: bridging the experimental length-scale gap, Scr. Mater. 143 (2018) 161–168. https://doi.org/10.1016/j.scriptamat.2017.04.026

[34] D. Terentyev, G. De Temmerman, T.W. Morgan, Y. Zayachuk, K. Lambrinou, B. Minov, A. Dubinko, K. Bystrov, G. Van Oost, Effect of plastic deformation on deuterium retention and release in tungsten, J. Appl. Phys. 117 (2015). https://doi.org/10.1063/1.4913478

[35] A. Dubinko, D. Terentyev, A. Bakaeva, T. Pardoen, M. Zibrov, T.W. Morgan, Effect of high flux plasma exposure on the micro-structural and -mechanical properties of ITER specification tungsten, Nucl. Instruments Methods Phys. Res. Sect. B Beam Interact. with Mater. Atoms. 393 (2017) 155–159. https://doi.org/10.1016/j.nimb.2016.10.041

[36] A. Dubinko, D. Terentyev, A. Bakaeva, M. Hernández-Mayoral, G. De Temmerman, L. Buzi, J.M. Noterdaeme, B. Unterberg, Sub-surface microstructure of single and polycrystalline tungsten after high flux plasma exposure studied by TEM, Appl. Surf. Sci. 393 (2017) 330–339. https://doi.org/10.1016/j.apsusc.2016.09.071

[37] S. Pathak, S.R. Kalidindi, Spherical nanoindentation stress-strain curves, Mater. Sci. Eng. R Reports. 91 (2015) 1–36. https://doi.org/10.1016/j.mser.2015.02.001

[38] J.S. Field, M. V Swain, R.D. Dukino, Determination of fracture toughness from the extra penetration produced by indentation-induced pop-in, J. Mater. Res. 18 (2003) 1412–1419. https://doi.org/10.1557/JMR.2003.0194

[39] S.-W. Jeon, K.-W. Lee, J.Y. Kim, W.J. Kim, C.-P. Park, D. Kwon, Estimation of Fracture Toughness of Metallic Materials Using Instrumented Indentation: Critical Indentation Stress and Strain Model, Exp. Mech. 57 (2017) 1013–1025. https://doi.org/10.1007/s11340-016-0226-2

[40] Q. Han, Z. Qu, P. Wang, G. Bi, G. Qu, Applications of Micro-Indentation Technology to Estimate Fracture Toughness of Shale, Materials (Basel). 13 (2020) 4208. https://doi.org/10.3390/ma13184208

[41] R.D. Dukino, M. V. Swain, Comparative Measurement of Indentation Fracture Toughness with Berkovich and Vickers Indenters, J. Am. Ceram. Soc. 75 (1992) 3299–3304. https://doi.org/10.1111/j.1151-2916.1992.tb04425.x

[42] W.Z. Yao, C.E. Krill, B. Albinski, H.C. Schneider, J.H. You, Plastic material parameters and plastic anisotropy of tungsten single crystal: A spherical micro-indentation study, J. Mater. Sci. 49 (2014) 3705–3715. https://doi.org/10.1007/s10853-014-8080-z

[43] X. Xiao, D. Terentyev, A. Ruiz, A. Zinovev, A. Bakaev, E.E. Zhurkin, High temperature nano-indentation of tungsten: Modelling and experimental validation, Mater. Sci. Eng. A. 743 (2019) 106–113. https://doi.org/10.1016/j.msea.2018.11.079

[44] X. Xiao, L. Chen, L. Yu, H. Duan, Modelling nano-indentation of ion-irradiated FCC single crystals by strain-gradient crystal plasticity theory, Int. J. Plast. 116 (2019) 216–231. https://doi.org/10.1016/j.ijplas.2019.01.005

[45] S. Dellis, X. Xiao, D. Terentyev, K. Mergia, S. Krimpalis, A. Bakaev, S. Messoloras, Mechanical properties of neutron-irradiated single crystal tungsten W(100) studied by indentation and FEM modelling, J. Nucl. Mater. (2021) 152985. https://doi.org/10.1016/j.jnucmat.2021.152985

[46] S. Bonk, J. Reiser, J. Hoffmann, A. Hoffmann, “cold” rolled tungsten (W) sheets and foils: Evolution of the microstructure, Int. J. Refract. Met. Hard Mater. 60 (2016) 92–98. https://doi.org/10.1016/j.ijrmhm.2016.06.020

[47] S. Krimpalis, K. Mergia, S. Messoloras, A. Dubinko, D. Terentyev, K. Triantou, J. Reiser, G. Pintsuk, Comparative study of the mechanical properties of different tungsten materials for fusion applications, Phys. Scr. T170 (2017) 014068. https://doi.org/10.1088/1402-4896/aa9292

[48] P. Lied, C. Bonnekoh, W. Pantleon, M. Stricker, A. Hoffmann, J. Reiser, Comparison of K-doped and pure “cold”-rolled tungsten sheets: As-rolled condition and recrystallization behaviour after isochronal annealing at different temperatures, Int. J. Refract. Met. Hard Mater. 85 (2019) 105047. https://doi.org/10.1016/j.ijrmhm.2019.105047

[49] D. Pelowitz, J. Durkee, J. Elson, M. Fensin, R. Johns, G. McKinney, S. Mashnik, J. Verbeke, L. Waters, T. Wilcox, MCNPX 2.7.0 Extensions, 2011

[50] R. Gröger, A.G. Bailey, V. Vitek, Multiscale modeling of plastic deformation of molybdenum and tungsten: I. Atomistic studies of the core structure and glide of 1/2〈111〉 screw dislocations at 0 K, Acta Mater. 56 (2008) 5401–5411. https://doi.org/10.1016/j.actamat.2008.07.018

[51] R. Hill, J.R. Rice, Constitutive analysis of elastic-plastic crystals at arbitrary strain, J. Mech. Phys. Solids. 20 (1972) 401–413. https://doi.org/10.1016/0022-5096(72)90017-8

[52] H. Lim, C.C. Battaile, J.D. Carroll, B.L. Boyce, C.R. Weinberger, A physically based model of temperature and strain rate dependent yield in BCC metals: Implementation into crystal plasticity, J. Mech. Phys. Solids. 74 (2015) 80–96. https://doi.org/10.1016/j.jmps.2014.10.003

[53] D. Hull, D.J. Bacon, Introduction to Dislocations, Elsevier, 2011. https://doi.org/10.1016/C2009-0-64358-0.

[54] A. Arsenlis, D.M. Parks, Modeling the evolution of crystallographic dislocation density in crystal plasticity, J. Mech. Phys. Solids. 50 (2002) 1979–2009. http://doi.org/10.1016/S0022-5096(01)00134-X

[55] D.J. Bacon, U.F. Kocks, R.O. Scattergood, The effect of dislocation self-interaction on the Orowan stress, Philos. Mag. 28 (1973) 1241–1263. https://doi.org/10.1080/14786437308227997

[56] Y.N. Osetsky, D.J. Bacon, An atomic-level model for studying the dynamics of edge dislocations in metals, Model. Simul. Mater. Sci. Eng. 11 (2003) 427–440. https://doi.org/10.1088/0965-0393/11/4/302

[57] Y.N. Osetsky, D.J. Bacon, V. Mohles, Atomic modelling of strengthening mechanisms due to voids and copper precipitates in α-iron, Philos. Mag. 83 (2003) 3623–3641. https://doi.org/10.1080/14786430310001603364

[58] Y.N. Osetsky, D.J. Bacon, Void and precipitate strengthening in α-iron: What can we learn from atomic-level modelling?, J. Nucl. Mater. 323 (2003) 268–280. https://doi.org/10.1016/j.jnucmat.2003.08.028

[59] D.J. Bacon, Y.N. Osetsky, Modelling dislocation-obstacle interactions in metals exposed to an irradiation environment, Mater. Sci. Eng. A. 400–401 (2005) 353–361. https://doi.org/10.1016/j.msea.2005.01.061

[60] D. Terentyev, D.J. Bacon, Y.N. Osetsky, Interaction of an edge dislocation with voids in α-iron modelled with different interatomic potentials, J. Phys. Condens. Matter. 20 (2008) 445007. https://doi.org/10.1088/0953-8984/20/44/445007

[61] Y.N. Osetsky, D.J. Bacon, Comparison of void strengthening in fcc and bcc metals: Large-scale atomic-level modelling, Mater. Sci. Eng. A. 400–401 (2005) 374–377. https://doi.org/10.1016/j.msea.2005.02.083

[62] E.O. Hall, The deformation and ageing of mild steel: II Characteristics of the Lüders deformation, Proc. Phys. Soc. Sect. B. 64 (1951) 742–747. https://doi.org/10.1088/0370-1301/64/9/302

[63] D. Terentyev, X. Xiao, A. Dubinko, A. Bakaeva, H. Duan, Dislocation-mediated strain hardening in tungsten: Thermo-mechanical plasticity theory and experimental validation, J. Mech. Phys. Solids. 85 (2015) 1–15. https://doi.org/10.1016/j.jmps.2015.08.015

[64] M. Birkholz, Thin Film Analysis by X-Ray Scattering, Wiley, 2005. https://doi.org/10.1002/3527607595

[65] T. Chudoba, F. Richter, Investigation of creep behaviour under load during indentation experiments and its influence on hardness and modulus results, Surf. Coatings Technol. 148 (2001) 191–198. https://doi.org/10.1016/S0257-8972(01)01340-8

[66] Z. Zhang, Y. Li, W. Wu, Effects of loading rate and peak load on nanoindentation creep behavior of DD407 Ni-base single crystal superalloy, Trans. Nonferrous Met. Soc. China 32(2022) 206−216. https://doi.org/10.1016/S1003-6326(21)65788-6

[67] Y. Wang, D. Raabe, C. Klüber, F. Roters, Orientation dependence of nanoindentation pile-up patterns and of nanoindentation microtextures in copper single crystals, Acta Mater. 52 (2004) 2229–2238. https://doi.org/10.1016/j.actamat.2004.01.016

[68] S. Chen, G. Gray, Constitutive behavior of tantalum and tantalum-tungsten alloys, Metall. Mater. Trans. A 27 (1996) 2994–3006, https://doi.org/10.1007/BF02663849

[69] M. Jahedi, M. Knezevic, M. Paydar, High-pressure double torsion as a severe plastic deformation process: experimental procedure and finite element modelling, J. Mater. Eng. Perform. 24 (2015) 1471–1482, https://doi.org/10.1007/s11665-015-1426-0

[70] M. Knezevic, M. Zecevic, I.J. Beyerlein, R.A. Lebensohn, A numerical procedure enabling accurate descriptions of strain rate-sensitive flow of polycrystals within crystal visco-plasticity theory, Comput. Methods Appl. Mech. Eng. 308 (2016) 468–482, https://doi.org/10.1016/j.cma.2016.05.025

[71] C. Yin, D. Terentyev, T. Zhang, S. Nogami, S. Antusch, C.C. Chang, R.H. Petrov, T. Pardoen, Ductile to brittle transition temperature of advanced tungsten alloys for nuclear fusion applications deduced by miniaturized three-point bending tests, Int. J. Refract. Met. Hard Mater. 95 (2021) 105464. https://doi.org/10.1016/j.ijrmhm.2020.105464